JOURNAL OF MATERIALS SCIENCE 28 (1993) 5775–5782

Effects of oxidation on intergranular phases in silicon nitride ceramics

M. K. CINIBULK, H.-J. KLEEBE
Max-Planck-Institut für Metallforschung, Institut für Werkstoffwissenschaft, D-7000 Stuttgart 1, Germany

The effects of oxidation on changes in the secondary phases of two Si_3N_4 ceramics were investigated by transmission electron microscopy. The Si_3N_4 materials were oxidized at 1400 °C for 168 h in laboratory air. One material, sintered with 5 vol % Yb_2O_3 + 0.5 vol % Al_2O_3, containing a $Yb_2Si_2O_7$ crystalline secondary phase, displayed no gross changes following oxidation. However, the thickness of the amorphous intergranular film was observed to have decreased by ~ 20% from its initial thickness of 1.0 nm. The second Si_3N_4 material, sintered with 5 wt % Y_2O_3 + 1 wt % MgO, had a completely amorphous secondary phase. Devitrification of the secondary phase at multiple-grain junctions to β-$Y_2Si_2O_7$ accompanied the outward diffusion of additive and impurity cations occurring in the residual amorphous intergranular films during oxidation. Substantial cavitation and intergranular phase depletion was observed at both multiple-grain junctions and two-grain boundaries. The equilibrium thickness of the amorphous intergranular film consequently decreased from 1.2 to 0.9 nm following oxidation. Purification of the amorphous intergranular films by diffusion of cations to the surface led to a reduction in impurity concentration, resulting in the observed thinning of grain-boundary films.

1. Introduction

Silicon nitride ceramics are being considered for use as structural components in high temperature oxidizing environments. Si_3N_4 is difficult to completely densify without the use of oxide additives that form an eutectic liquid through which mass transport, and hence the sintering process, is enhanced. It is the residual liquid following densification that forms the intergranular phase in Si_3N_4 ceramics, on which the high-temperature behaviour of these materials depends. Although studies [1–6] have shown that the bulk of this intergranular phase can be crystallized by a post-sintering heat treatment, there remains a thin amorphous film at the grain boundaries. Clarke [7] has proposed that the existence of this amorphous film is an equilibrium phenomenon, due to a balance between the attractive van der Waals forces between the grains and a repulsive steric force resulting from resistance to deformation of the SiO_4^{4-} tetrahedra in the silicate phase. Based on an electron diffraction study of glass at two-grain boundaries and triple-grain junctions in sintered alumina/anorthite, Marion *et al.* [8] suggested that the two-grain boundary films were more highly ordered that the glass at the multiple-grain junctions, supporting the theory of "stress-supporting entities" that could provide a repulsive force. A second model predicting a stable viscous intergranular film was developed by Kwon and Messing [9], which is based on a hydrostatically squeezed film that can support the normal stress arising from the force due to the curved liquid-vapour interface (Laplacian force) acting to draw the grains together during solution–reprecipitation. Clarke *et al.* [10] recently proposed another model to explain the stability of these films, which is based on the presence of an electrical double layer at the interface. In all of the proposed models the thickness of the grain-boundary film is determined primarily by the chemical composition of the system. The dependence of the grain-boundary film thickness on various sintering additives (and hence chemical composition) of Si_3N_4 ceramics was recently demonstrated by the authors [11, 12]. The thickness of the amorphous grain-boundary film was found to depend on the M/Si ratio (where M is total cations present) of the amorphous phase [11].

In addition to the dependence of the amorphous film on different compositions of the liquid phase (e.g. sintering with Y_2O_3 versus CeO_2), the film thickness is expected to depend on the presence of minor impurities as well. Most of the impurities in commercially available Si_3N_4 powders act as random-network formers to enhance the stability of the amorphous phase, and are believed to contribute in part to incomplete crystallization of the secondary phase at multiple-grain junctions [3–5, 13, 14]. As devitrification of the secondary phase proceeds, the impurities that are not accommodated in the structure of the crystalline phase(s) by solid solution are excluded to the residual amorphous phase where their concentration is increased. The concentration of these impurities in the

0022–2461

residual amorphous phase then becomes a factor in determining liquid composition and, hence, grain-boundary film thickness.

The oxidation behaviour of Si_3N_4 ceramics is directly influenced by the composition and crystalline state of the secondary phase. High-temperature exposure of liquid-phase sintered silicon nitride leads to accelerated oxidation, attributable to the enhanced oxidation of Si_3N_4 dissolved in the viscous silicate phase present at the surfaces [15]. Cubicciotti and Lau [16] showed that the outward diffusion of additive cations (e.g. Mg^{2+}, as well as impurities such as Al^{3+}, Ca^{2+} and Fe^{3+}) and nitrogen, produced by the amorphous intergranular-phase/oxide layer diffusion couple, and the inward diffusion of oxygen resulted in a compositional gradient beneath the oxide layer. The presence of residual amorphous grain-boundary phases, which are not in equilibrium with SiO_2 (the oxidation product of Si_3N_4), results in the creation of a driving force for additive and impurity cation diffusion to the Si_3N_4-bulk/oxide-layer interface. Therefore, during oxidation the residual amorphous phase is in essence being purified and the chemistry of the intergranular film is expected to shift to a lower M/Si ratio, along with a decrease in grain-boundary film thickness. This paper discusses the effects of oxidation on the microstructure of two Si_3N_4 materials containing different secondary phases, with emphasis on changes occurring in the amorphous grain-boundary films, as observed by transmission electron microscopy (TEM).

2. Experimental procedure

The materials used in this study were two silicon nitride ceramics, each consisting of a different secondary phase. One material was sintered with 5 vol % Yb_2O_3, plus an additional 0.5 vol % Al_2O_3 added for enhanced sinterability, at 1800 °C for 2 h under 0.1 MPa N_2 [6]. Following densification this composition underwent a 12 h heat treatment at 1250 °C under 0.1 MPa N_2 to devitrify the secondary phase. The second Si_3N_4 material was produced by reaction-bonding Si and N_2 in the presence of 5 wt % Y_2O_3 + 1 wt % MgO, followed by the application of a two-step gas-pressure sintering technique to achieve full density. The material was first heated to 1875 °C and held for 90 min under 0.5 MPa N_2, followed by a 60 min hold at 1925 °C under 10 MPa N_2. No heat treatment was applied and a completely amorphous secondary phase was obtained.

Two 3 mm diameter TEM specimens were prepared from each Si_3N_4 material and mechanically thinned to ~ 0.5 mm. One sample from each composition was then oxidized in laboratory air at 1400 °C for a period of 168 h. The second specimen from each composition was retained in the as-processed (non-oxidized) state. The four materials are designated as follows: Yb/A (5 vol % Yb_2O_3 + 0.5 vol % Al_2O_3/Si_3N_4, annealed in N_2), Yb/AO (5 vol % Yb_2O_3 + 0.5 vol % Al_2O_3/Si_3N_4, annealed in N_2, and then oxidized), Y/S (5 wt % Y_2O_3 + 1 wt % MgO/Si_3N_4, as-sintered) and Y/O (5 wt % Y_2O_3 + 1 wt % MgO/Si_3N_4 oxidized). All four samples were then mechanically thinned to 100 μm. The foils were further thinned in the center to ~ 10 μm by dimpling, followed by ion beam thinning to electron transparency. The TEM foils were finally coated with a thin layer of carbon to minimize charging under the electron beam.

Conventional TEM and analytical electron microscopy (AEM) were performed using a JEOL JEM-2000FX operated at 200 kV, equipped for energy-dispersive X-ray spectroscopy (EDS) with an ultra-thin window germanium detector. To accurately determine the nature and thickness of the intergranular films at two-grain boundaries, high-resolution electron microscopy (HREM) was carried out at 400 kV on a JEOL JEM-4000EX (0.18 nm point-to-point resolution).

3. Results

3.1. General microstructures

3.1.1. As-processed materials

Descriptions of the general microstructures, including secondary-phase characterization, of the two oxidized and two non-oxidized materials are summarized in Table I. The microstructures of all four materials consisted of β-Si_3N_4 grains surrounded by a secondary phase composed primarily of the oxide additives. Sample Yb/A had a very fine grain size, shown in Fig. 1(a), with the majority of grains having diameters (measured across the basal plane) of ~ 0.1–0.4 μm and a low aspect-ratio grain morphology. The secondary phase was nearly completely crystallized as a result of the 12 h heat treatment at 1250 °C, confirming the results of a recent study [6] on this material. Fig. 2(a) shows the microstructure of sample Yb/A with a secondary phase of $Yb_2Si_2O_7$, along with pockets of residual amorphous phase. The residual amorphous regions at the multiple-grain junctions were rarely observed, and EDS [Fig. 2(b)] indicated

TABLE I General microstructural features of the Si_3N_4 ceramics

Material[a]	β-Si_3N_4 grain diameter (μm)	Secondary phase	
		As-processed	Oxidized
Yb/A	0.1–0.4	$Yb_2Si_2O_7$ < 5% amorphous	$Yb_2Si_2O_7$ < 1% amorphous
Y/S	0.5–1.5	Amorphous MgYSiON	β-$Y_2Si_2O_7$, cavities with residual amorphous film

[a] Yb/A: 5 vol % Yb_2O_3 + 0.5 vol % Al_2O_3/Si_3N_4, annealed in N_2. Y/S: 5 wt % Y_2O_3 + 1 wt % MgO/Si_3N_4, as-sintered.

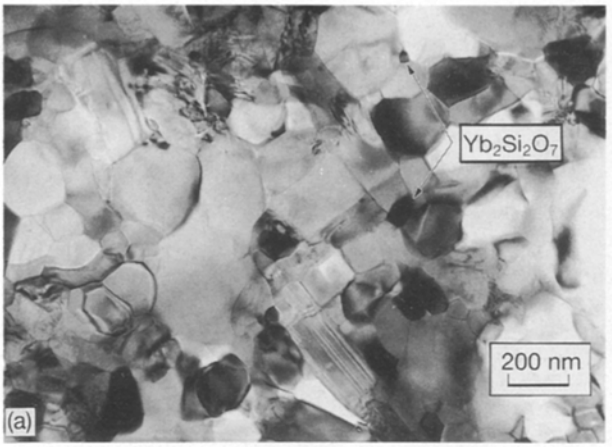

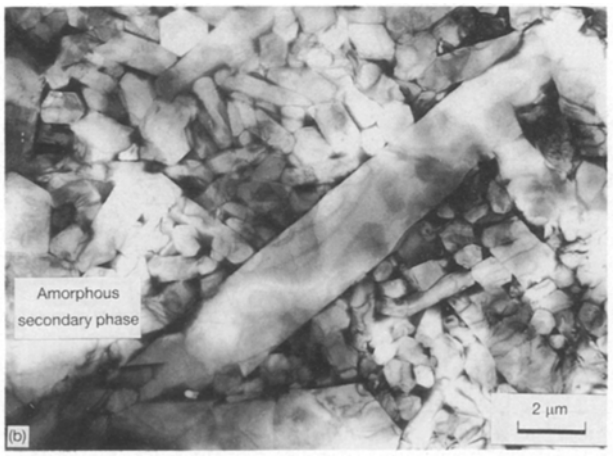

Figure 1 TEM micrographs of (a) sample Yb/A and (b) sample Y/S showing the general microstructures and grain morphologies. Note the much finer and globular shaped grains of sample Yb/A, shown in (a).

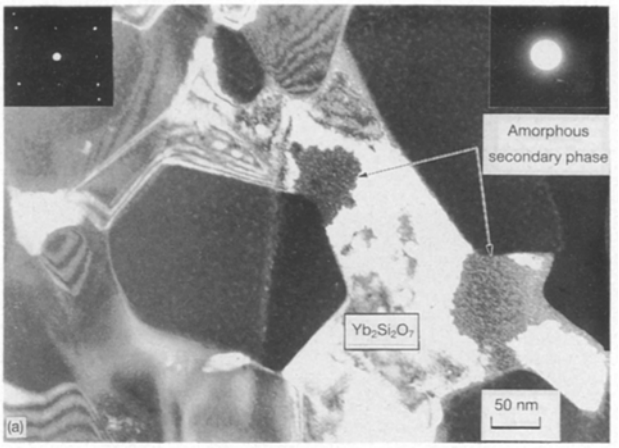

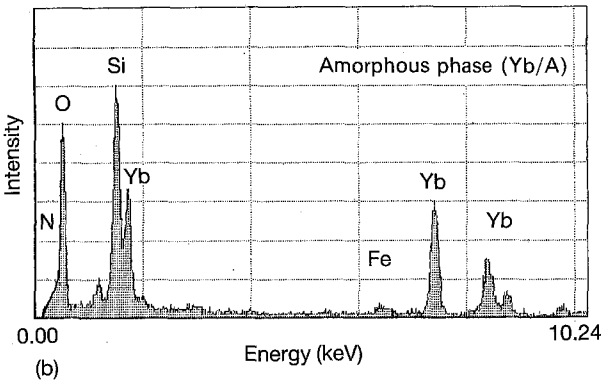

Figure 2 (a) TEM dark-field image showing the crystalline secondary phase of sample Yb/A in bright contrast and residual pockets of amorphous phase. Top left inset is the diffraction pattern identifying $Yb_2Si_2O_7$ as the secondary phase, here in the [1 1 2] orientation. Top right inset is the microdiffraction pattern of the amorphous pockets. (b) EDS spectrum of the residual amorphous phase.

that these regions had a lower Yb/Si ratio than $Yb_2Si_2O_7$. The presence of Al in any Yb-containing phases could not be determined due to the overlap of the AlK_α peak and YbM_α peak. Microanalysis of β-Si_3N_4 grains indicated that they contained ~ 1 at % Al in solid-solution. Fe-rich inclusions were also observed to be present at the grain boundaries, composed primarily of Fe, Si, Cr and Ni.

Sample Y/S had a much larger grain size [Fig. 1(b)], which consisted of elongated β-Si_3N_4 grains of ~ 0.5–1.5 μm diameter (across the basal plane), with aspect ratios of up to 10. The secondary phase was completely amorphous, as shown in Fig. 3(a), with a homogeneous composition as determined by X-ray microanalysis [Fig. 3(b)]. The secondary phase was composed of approximately 15 at % N, 47 at % O, 5.5 at % Mg, 0.5 at % Al, 18 at % Si and 14 at % Y. As indicated, Al was detected as the major impurity along with traces of Ca and Fe (< 0.2 at %).

3.1.2. Oxidized materials

Following the 168 h oxidation at 1400 °C, the colour of both materials had noticeably lightened from dark grey to light grey. This lightening in colour was observed in the centre of the samples as well, following the second dimpling during TEM specimen preparation. The oxidized surfaces of sample Yb/AO were macroscopically smooth, while the oxidized surfaces of sample Y/O were rougher and bloated, as has been reported of oxidized MgO-sintered Si_3N_4 [15, 16].

No obvious changes occurred to the general microstructure of sample Yb/AO following oxidation. The secondary phase consisted of $Yb_2Si_2O_7$ prior to oxidation and, therefore, no change would be expected to occur to this phase during oxidation since it is in equilibrium with SiO_2 [17]. The high oxidation resistance of this material can be attributed to the presence and stability of $Yb_2Si_2O_7$ as the secondary phase.

The lower oxidation resistance of sample Y/O was evident from the changes in the state of the secondary phase. Glass that once occupied the multiple-grain junctions had either crystallized or diffused out of the pockets. Fig. 4 shows the changes observed in the secondary phase of sample Y/O after oxidation. Where the amorphous secondary phase had devitrified the product was β-$Y_2Si_2O_7$, exclusively. A small fraction of the secondary phase had diffused out of the material, leaving many pockets empty with only thin residual amorphous layers lining the cavities. These layers were always found to be rich in Fe and depleted of both Mg and Y, as shown in Fig. 4(b). Occasionally inclusions were observed at the multiple-grain junctions that were composed of various metallic impurities. The inclusions were not all of the same chemical

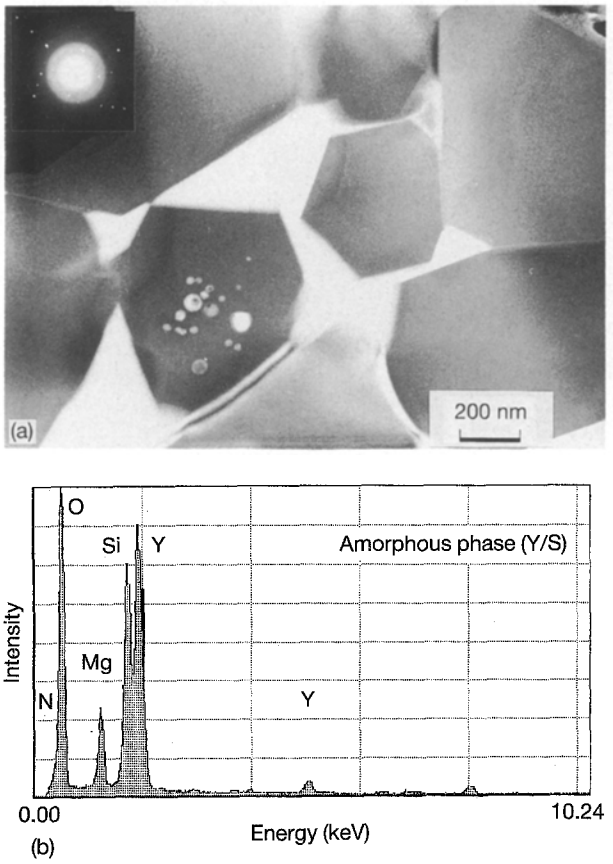

Figure 3 (a) Diffuse dark-field image of sample Y/S, showing the amorphous secondary phase in bright contrast. Inset is the corresponding microdiffraction pattern of the amorphous phase. (b) EDS spectrum of the amorphous secondary phase.

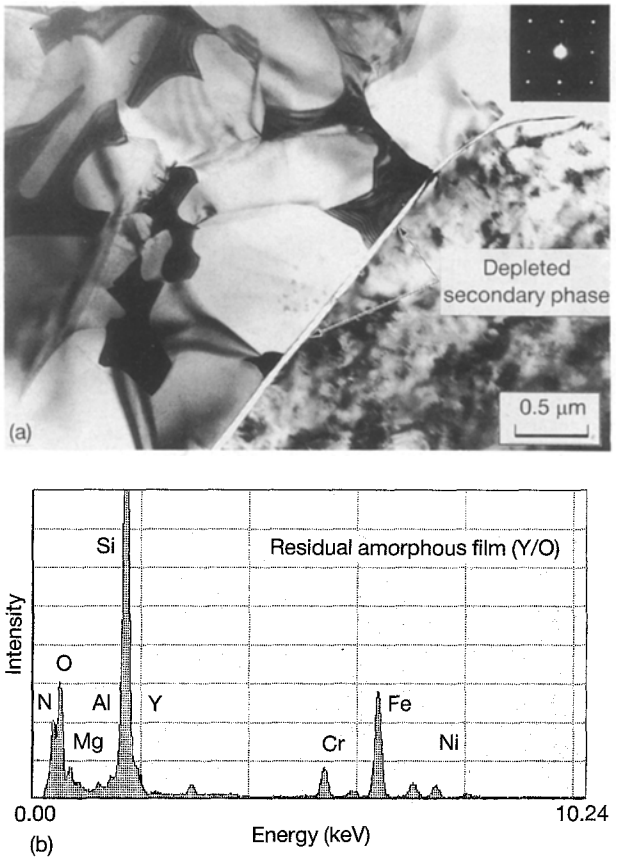

Figure 4 (a) Bright-field image of sample Y/O showing the depletion of intergranular phase, which is observed at triple-junctions as well as two-grain boundaries, following oxidation. The large Si_3N_4 grain in the lower-right-third of the image is oriented along the [0001] zone axis. Inset is the diffraction pattern of β-$Y_2Si_2O_7$, which crystallized at the majority of multiple-grain junctions (dark contrast), oriented in the [100] direction, (b) EDS spectrum of the residual amorphous layer at the depleted grain boundary.

composition, with some being primarily Ca, Fe and Mg, other containing mainly Ti and Al, and a minority composed of Ba, K, Ca and Fe. A small amount of Si_2N_2O was also detected and assumed to be the result of the secondary phase devitrification as the additive and impurity cation content decreased and the oxygen concentration increased, as well as due to the reaction of Si_3N_4 with SiO_2.

3.2. Amorphous grain-boundary films

To examine the effects of oxidation on the amorphous grain-boundary films in these materials it was necessary to use high-resolution electron microscopy. Based on the results of a recent study [18] comparing the various techniques used in the examination of grain boundaries in ceramic materials, high-resolution lattice imaging was used to quantitatively determine the intergranular film thickness of the two silicon nitrides to $\pm$ 0.1 nm, before and after oxidation. Diffuse dark-field imaging and defocus Fresnel fringe imaging were used primarily to locate amorphous phases and to assist in orienting grain boundaries parallel to the electron beam for thickness determination, respectively.

3.2.1. As-processed materials

Both of the materials examined contained thin amorphous grain-boundary films prior to and after oxidation. Fig. 5 contains an HREM image of a

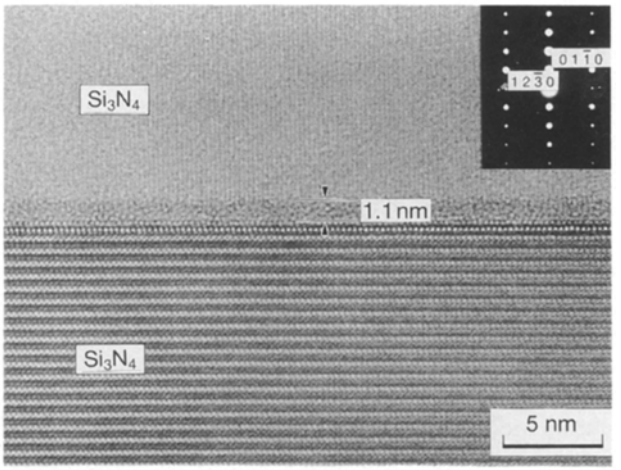

Figure 5 HREM image of a β-Si_3N_4/β-Si_3N_4 grain boundary in sample Yb/A showing the equilibrium amorphous film thickness.

β-Si_3N_4/β-Si_3N_4 grain boundary in sample Yb/A. From measurements obtained from a number of similar micrographs of different grain boundaries (using the $\{10\bar{1}0\}$ lattice fringes (0.66 nm interplanar spacing) as an internal standard) an intergranular film thickness of 1.0 nm was found to characterize this material. All grain boundaries were observed to be

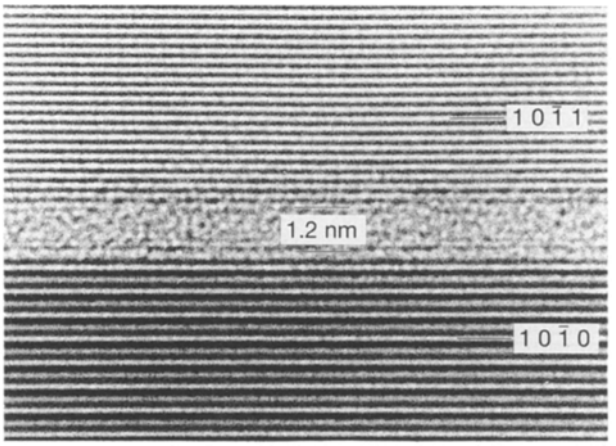

Figure 6 HREM image of a β-Si_3N_4/β-Si_3N_4 grain boundary in sample Y/S, showing the equilibrium amorphous film thickness.

wetted by an amorphous film of 1.0 ± 0.1 nm in thickness, with the exception of a few low-angle grain boundaries which were free of any intergranular film.

Measurements of intergranular films from HREM images of sample Y/S, such as that in Fig. 6, indicate a characteristic thickness of 1.2 nm. Every grain boundary was observed to contain an amorphous film of 1.2 ± 0.1 nm in thickness, with the exception of the low-angle grain boundaries previously mentioned. This value is consistent with the trend in film thicknesses of 1.0 nm and 1.5 nm observed in Si_3N_4 sintered with 1 wt % Y_2O_3 + 0.2 wt % Al_2O_3 and 10 wt % Y_2O_3 + 2 wt % Al_2O_3, respectively, where the M/Si ratio is correspondingly increased [11].

3.2.2. Oxidized materials

Although the general microstructure of sample Yb/AO remained unchanged following oxidation, HREM of the intergranular films revealed changes occurring at the grain boundaries. HREM imaging of grain boundaries in this material was complicated by the very fine size and non-equilibrium shape of the grains, in conjunction with the presence of a very thin amorphous film. The amorphous film thickness at β-Si_3N_4/β-Si_3N_4 grain boundaries is believed to have decreased following oxidation. Fig. 7 shows two grain boundaries in sample Yb/AO with an intergranular film thickness of somewhat less than the 1.0 nm film thickness observed in the non-oxidized material. Because the grain boundaries in Fig. 7 are curved in the plane, as well as out of the plane, of the micrograph, it is not possible to obtain an interface with planar edges parallel to the electron beam, i.e. there will always be some degree of overlap of the amorphous film with the Si_3N_4 grains. Therefore, the thickness of these films can only be estimated to be less than those observed in the same material prior to oxidation. The reduction in film thickness is expected, due to a lowering in the M/Si ratio following amorphous phase purification via oxidation.

Examination of interfaces in sample Y/O by HREM resulted in the detection of four types of grain boundaries. The first type was characterized as a low-energy grain boundary, free of any amorphous intergranular

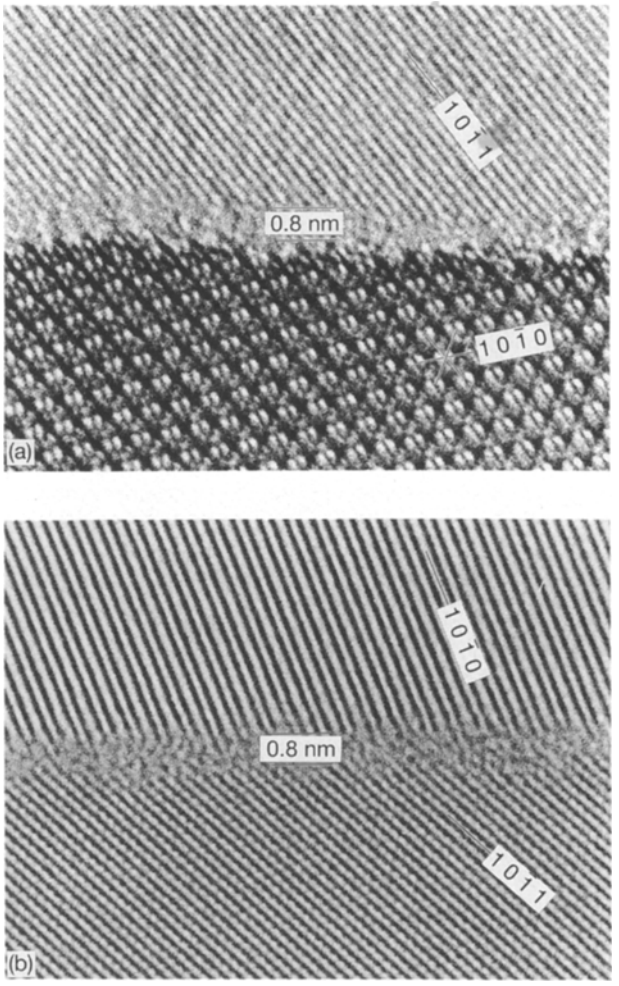

Figure 7 HREM images showing apparent thinning of the intergranular film at two β-Si_3N_4/β-Si_3N_4 grain boundaries in sample Yb/AO. Curvature of the interfaces complicates precise intergranular film thickness determination in this material.

film, shown in Fig. 8(a). The second type was that observed at β-Si_3N_4/β-Si_3N_4 grain boundaries, shown in Fig. 8(b). The amorphous film thickness was found to have decreased from 1.2 nm in the non-oxidized material to 0.9 nm in the same material following oxidation. The third type of grain boundary was formed as a result of devitrification of the secondary phase during oxidation. Heterophase boundaries between β-Si_3N_4 and β-$Y_2Si_2O_7$ contained amorphous films ~ 3.0 nm in width, shown in Fig. 8(c). The fourth type of interface observed consisted of a wide zone separating the two β-Si_3N_4 grains, as can be seen in Fig. 9. The separation of β-Si_3N_4 grains at different grain boundaries was found to vary from ~ 4.0 nm to ~ 7.0 nm in width. The intergranular region is believed to be composed of a single amorphous phase that is coating each of the β-Si_3N_4 grains, separated by a microcrack. The depleted region, which is void of any material, is seen in Fig. 9(a) to be filled by the amorphous carbon deposited on the surface of the specimen to avoid charging. The width of this boundary is a factor of ~ 7 times greater than that of "normal" β-Si_3N_4/β-Si_3N_4 grain boundaries observed in this oxidized material. Fig. 9(b) is a micrograph of the same interface imaged with a defocused objective lens (Δf = − 500 nm) which results in the formation

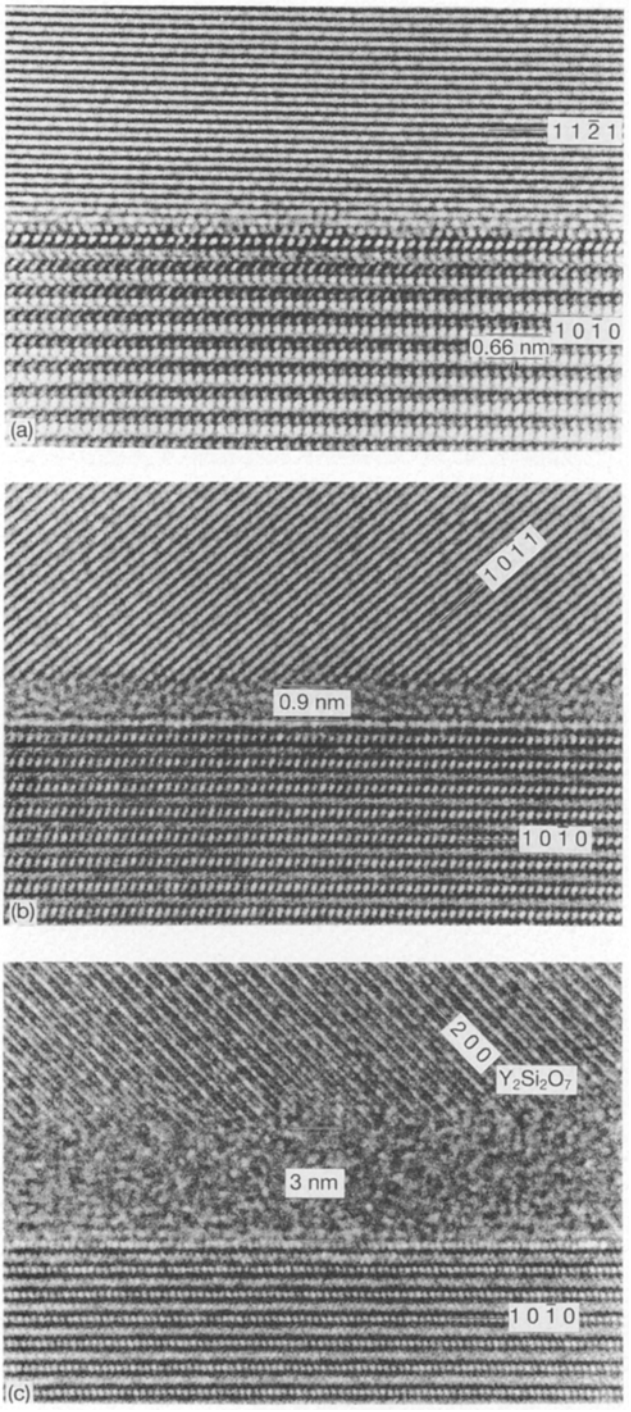

Figure 8 HREM images of the types of grain boundaries observed in sample Y/O. (a) Low-energy β-Si_3N_4/β-Si_3N_4 grain boundary with no observable intergranular film. (b) Intergranular film of reduced thickness at a β-Si_3N_4/β-Si_3N_4 grain boundary. (c) Intergranular film at a β-$Y_2Si_2O_7$/β-Si_3N_4 grain (phase) boundary.

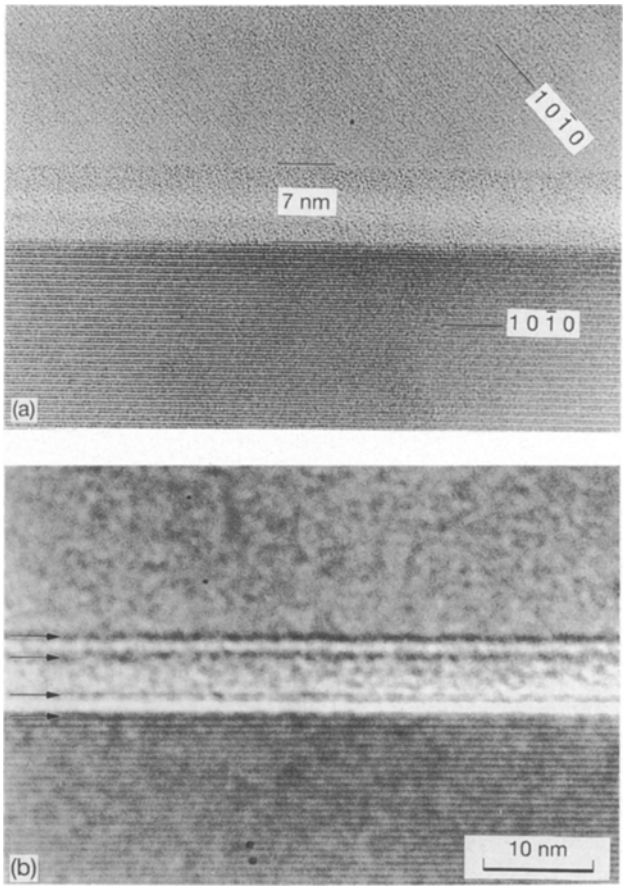

Figure 9 (a) HREM image of two β-Si_3N_4 grains separated by a depleted zone in the centre, with an oxide film at the grain surfaces. The oxide film (in darker contrast) on the grains is ~ 2.5 nm thick, with the depleted zone (central region in brighter contrast) being ~ 2.0 nm wide. (b) Defocused image ($\Delta f = -500$ nm) of the same grain boundary showing Fresnel fringes (arrowed) at β-Si_3N_4/amorphous film interfaces, as well as at amorphous film/depleted zone (carbon coating) interfaces.

of Fresnel fringes at the interface of materials having different mean inner potentials [18]. The double set of Fresnel fringes are seen at the β-Si_3N_4/amorphous film interfaces as well as the amorphous film/carbon coating (depleted zone) interfaces, indicating the presence of four distinct interfaces and supporting the interpretation of a depleted grain boundary. The ~ 2.5 nm thick amorphous films coating the β-Si_3N_4 grains are believed to be oxide products resulting from direct oxidation of the surfaces following intergranular film depletion and crack propagation. A similar grain-boundary feature has been observed in SiC when the interface is penetrated by a microcrack [19]. The SiC grains were observed to have been separated by the microcrack, which was covered by the carbon coating, and an amorphous oxide layer that had formed on the SiC surfaces after penetration of the microcrack.

4. Discussion

Changes in the intergranular phases of these silicon nitride materials during oxidation can be attributed to both the establishment of a simple heat treatment in air during which devitrification of the amorphous phase occurs and to a chemical potential gradient (due to surface oxidation) that leads to changes in the chemical composition of the amorphous phase. For the case of the Yb_2O_3-sintered Si_3N_4 that had been annealed in nitrogen to devitrify the secondary phase, little further crystallization of the intergranular phase probably occurred. Since the devitrification product during annealing was $Yb_2Si_2O_7$, which is stable toward oxidation, no reactions or phase transformations involving this phase were expected or observed. The only observable difference between the secondary phases of this material prior to and after

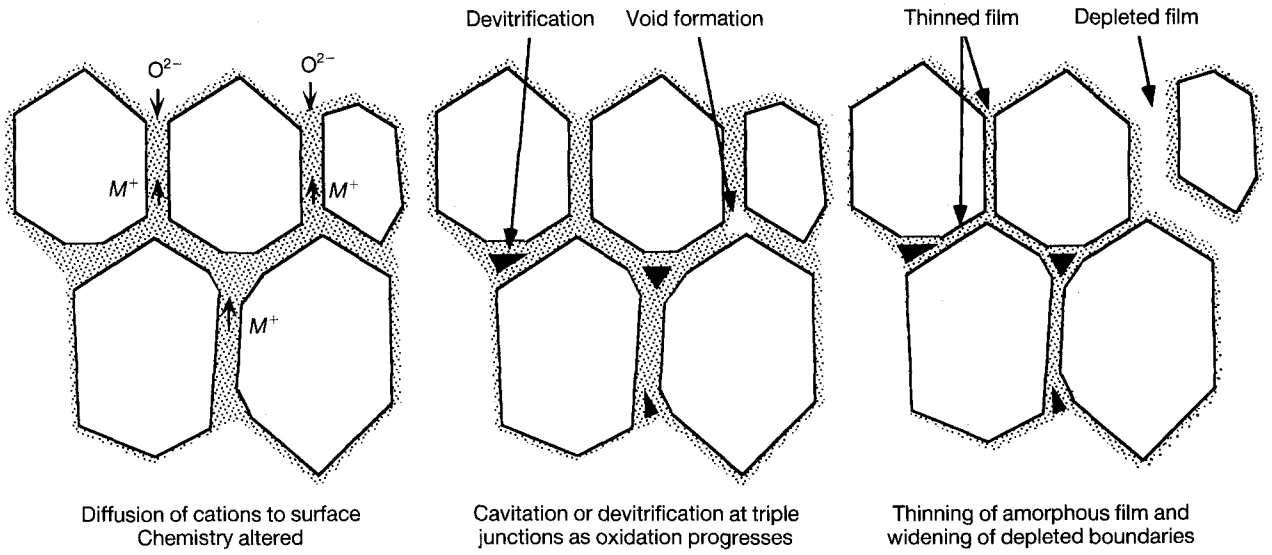

Figure 10 Schematic of the observed effects of high-temperature oxidation on the intergranular phase of sample Y/O. M^+ represents all additive and impurity cations present.

oxidation was the thickness of the residual amorphous film, which appeared to have decreased. The difference in film thickness on this order of magnitude is difficult to determine with absolute certainty, due to the error of $\pm$ 0.1 nm that is associated with each measurement of the intergranular phase from HREM micrographs. The difference in film thickness is believed to be attributable to a decrease in additive and impurity cation concentration in the residual amorphous phase, which lowers the *M*/Si ratio and results in a decreased intergranular film thickness. The opposite effect has recently been observed when impurities are *added* to this material in a controlled manner [20]. The addition of 0.25 vol % CaO to sample Yb/A resulted in the incorporation of Ca^{2+} in the amorphous intergranular phase, which led to an increase in the film thickness from 1.0 to 1.3 nm.

These observations can be explained using Clarke's model [7]. For an amorphous film of pure silica glass the equilibrium film thickness is determined by the balance between the van der Waals dispersion force, between the grains acting to thin the film, and the repulsive steric force, due to the structure of the glass. The inclusion of impurity cations in the glass may lead to the formation of an electrical double layer at the grain boundaries that could contribute an additional repulsive force [10]. Oxidation results in a decrease in impurity cation concentration in the intergranular glass, leading to a reduction in the entropic repulsive force by the electrical double layer. Therefore, the purification of the intergranular phase will result in a decrease in film thickness, as observed in the oxidized materials, while the incorporation of additional impurities will result in an increase in the amorphous film thickness.

To further explore the effects of oxidation on these materials, the second Si_3N_4-based composition was oxidized and examined. Sample Y/S was chosen because it contained MgO as a sintering additive and because it consisted of large equilibrium-shaped β-Si_3N_4 grains, which results in planar interfaces that are needed for precise intergranular film thickness measurements. Mg^{2+} is expected to readily diffuse through the amorphous phase during oxidation, producing a greater change in the *M*/Si ratio in the intergranular films of this material as compared with sample Yb/A. The intergranular film thickness of sample Y/S was also expected to be greater than that of Yb/A [11], which should make changes in the film thickness more readily observable.

The changes in the secondary phase from oxidation of the Y_2O_3 + MgO-sintered Si_3N_4 were due to a combination of devitrification of the secondary phase and purification of the residual amorphous phase, resulting in a quantifiable reduction in amorphous intergranular film thickness [compare Figs 6 and 9(b)]. A schematic of the changes occurring in this material is given in Fig. 10; the process leading to the observed changes in intergranular phases is proposed as follows. During the initial exposure of this material to 1400 °C in air, crystallization of the intergranular phase to β-$Y_2Si_2O_7$ begins and oxidation of the surface takes place leading to a driving force for cation diffusion to the surface oxide scale. As the secondary phase at the majority of multiple-grain junctions devitrifies and outward diffusion of additive and impurity cations continues, cavitation occurs at some of the multiple-grain junctions where the amorphous phase is more volatile, probably due to a higher concentration of impurities in these locations. The cavitation continues in these areas, depleting the multiple-grain junctions of amorphous material as cations continue to diffuse to the oxide surface and oxygen diffuses into the material via the amorphous grain-boundary films. The chemical change taking place in the residual amorphous films due to outward diffusion of cations decreases the *M*/Si ratio, resulting in a thinning of the intergranular film thickness. As the majority of grain boundaries thin, due to compositional change in the intergranular phase, tensile stresses are imposed on those grain boundaries where depletion of the amorphous film has begun. Additional tensile stresses can arise from the presumed volume contraction at the multiple-grain junctions due to crystallization of

the intergranular phase (assuming that the devitrified product has a higher density than the glass). Complete depletion of these grain boundaries then results as they are separated to relieve the tensile stresses, resulting in microcracking and further oxidation of the Si_3N_4 surfaces within the bulk.

5. Conclusions

The effects of oxidation on the secondary intergranular phases of two Si_3N_4 ceramics were investigated by TEM and found to depend on the composition and state (crystalline or amorphous) of the secondary phases. In sample Yb/A, which contained nearly completely crystallized multiple-grain junctions prior to oxidation, the presence of $Yb_2Si_2O_7$ as the major secondary phase results in a very oxidation resistant material. The residual amorphous intergranular film detected at the grain boundaries was determined, from HREM micrographs, to be 1.0 ± 0.1 nm thick prior to oxidation. During the 1400 °C exposure to air for 168 h the diffusion of additive and impurity cations from the amorphous phase to the surface oxide layer and inward diffusion of oxygen along the amorphous intergranular films results in a modification of the amorphous phase composition. The M/Si ratio is decreased, which is accompanied by an apparent decrease in the intergranular film thickness.

In sample Y/S, which consisted of a completely amorphous secondary phase, devitrification of the amorphous phase at multiple-grain junctions to β-$Y_2Si_2O_7$ accompanies the diffusional process occurring in the residual amorphous intergranular films during oxidation. Substantial cavitation and amorphous phase depletion was observed at both multiple-grain junctions and two-grain boundaries, which is attributable to the lower viscosity of the amorphous phase present in this material and its greater susceptibility to oxidation. The equilibrium thickness of the amorphous intergranular film decreased from 1.2 to 0.9 nm following oxidation.

The amorphous intergranular film thickness has been shown to depend on its chemical composition, and small amounts of impurities can effect the forces responsible for determining its equilibrium thickness. If upon devitrification of the bulk of the glass at multiple-grain junctions, high-temperature behaviour depends primarily on the viscosity and thickness of the residual amorphous grain-boundary films, careful post-processing oxidation could result in improvements in mechanical properties by purification and thinning of these films. Although this study was limited to two materials, similar microstructural changes are expected to take place in other Si_3N_4-based materials, which will depend primarily on the composition and state of the secondary phase. For materials where the secondary phase has been appropriately tailored for high temperature oxidizing conditions by obtaining thermodynamically stable crystalline phases and refractory residual amorphous phases, deleterious changes in composition and microstructure can be minimized during exposure.

Acknowledgements

We thank M. J. Hoffmann for supplying the Yb_2O_3-sintered Si_3N_4 material and for the use of the high-temperature furnace for the oxidation procedure.

References

1. A. TSUGE, K. NISHIDA and M. KOMATSU, *J. Amer. Ceram. Soc.* **58** (1975) 323.
2. D. A. BONNELL, T.-Y. TIEN and M. RÜHLE, *ibid.* **70** (1987) 460.
3. L. K. L. FALK and G. L. DUNLOP, *J. Mater. Sci.* **22** (1987) 4369.
4. M. K. CINIBULK, G. THOMAS and S. M. JOHNSON, *J. Amer. Ceram. Soc.* **73** (1990) 1606.
5. *Idem., ibid.* **75** (1992) 2037.
6. J. S. VETRANO, H.-J. KLEEBE, E. HAMPP, M. J. HOFFMANN, R. M. CANNON and M. RÜHLE, *J. Mater. Sci.* (in review).
7. D. R. CLARKE, *J. Amer. Ceram. Soc.* **70** (1987) 15.
8. J. E. MARION, C. H. HSUEH and A. G. EVANS, *ibid.* **70** (1987) 708.
9. O.-H. KWON and G. L. MESSING, *Acta. Metall. Mater.* **39** (1991) 2059.
10. D. R. CLARKE, T. M. SHAW and A. P. PHILIPSE and R. G. HORN *J. Amer. Ceram. Soc.* **76** (1993) 1201.
11. H.-J. KLEEBE, *J. Europ. Ceram. Soc.* (in press).
12. H.-J. KLEEBE and M. K. CINIBULK, *J. Mater. Sci. Lett.* **12** (1993) 70.
13. R. E. LOEHMAN and D. J. ROWCLIFFE, *J. Amer. Ceram. Soc.* **6** (1980) 144.
14. W. BRAUE, G. WÖTTING and G. ZIEGLER, in "Ceramic microstructures '86: role of interfaces", edited by J. A. Pask and A. G. Evans (Plenum Press, New York, 1987) p. 883.
15. S. C. SINGHAL, *J. Mater. Sci.* **11** (1976) 500.
16. D. CUBICCIOTTI and K. H. LAU, *J. Amer. Ceram. Soc.* **61** (1978) 512.
17. M. K. CINIBULK, G. THOMAS and S. M. JOHNSON, *ibid.* **75** (1992) 2044.
18. M. K. CINIBULK, H.-J. KLEEBE and M. RÜHLE, *ibid.* **76** (1993) 426.
19. H.-J. KLEEBE and A. G. EVANS, (1990).
20. H.-J. KLEEBE, J. BRULEY and M. RÜHLE, *J. Mater. Res.* (in review).

Received 2 June 1992
and accepted 24 February 1993